Numerical simulation of fluid–solid interaction using an immersed boundary finite element method

Ilinca, F.; Hétu, J.-F.

Publisher's version / Version de l'éditeur:
https://doi.org/10.1016/j.compfluid.2012.02.008
Computers & Fluids, 59, pp. 31-43, 2012-02-24

Numerical simulation of fluid-solid interaction using an immersed boundary finite element method

F. Ilinca and J.-F. Hétu

National Research Council, 75 de Mortagne, Boucherville, Qc, Canada, J4B 6Y4

Abstract

This paper presents applications of a recently proposed immersed boundary method to the solution of fluid-solid interaction. Solid objects immersed into the fluid are considered rigid and their movement is either imposed or determined from the interaction forces with the fluid. The use of body-conforming meshes to solve such problems may involve extensive mesh adaptation work that has to be repeated each time a change in the shape of the domain or in the position of immersed solids is needed. Mesh generation and solution interpolation between successive grids may be costly and introduce errors if the geometry changes significantly during the course of the computation. These drawbacks are avoided when the solution algorithm can tackle grids that do not fit the shape of immersed objects. We present here an extension of our recently developed Immersed Boundary (IB) finite element method to the computation of interaction forces between the fluid and immersed solid bodies. A fixed mesh is used covering both the fluid and solid regions, and the boundary of immersed objects is defined using a time dependent level-set function. Boundary conditions on the immersed solid surfaces are imposed accurately by enriching the finite element discretization of interface elements with additional degrees of freedom which are latter eliminated at element level. The forces acting on the solid surfaces are computed from the enriched finite element solution and if needed the solid movement is determined from the rigid solid momentum equation. Solutions are shown for various fluid-solid interaction problems and the accuracy of the present approach is measured with respect to solutions on body-conforming meshes.

Keywords: Immersed boundary method, Fluid-solid interaction, Finite elements, Non body-conforming mesh, Pressure enrichment

1. INTRODUCTION

Most CFD and fluid-structure interaction solvers are based on body-conforming (BC) grids (i.e. the external boundary and surfaces of immersed bodies are represented by the mesh faces), but there is an increased interest in solution algorithms for non body-conforming grids. Such methods are reported under a variety of appellations: immersed boundary, immersed interface, embedded mesh, fictitious domain, all having in common the fact that the spatial discretization is done over a single domain containing both fluid and solid regions and where mesh points are not necessarily located on the fluid-solid interface. For simplicity, we will use in the present work the immersed boundary (IB) term to identify a non body-fitted method. IB methods have the main advantage of avoiding costly and sometimes very difficult meshing work on body-fitted geometries. Generally a regular parallelepiped is meshed with an uniform grid. The IB method results also in important algorithmic simplifications when immersed moving bodies are considered. One important drawback of such a method is that the boundary which has an important influence on the solution especially for fluid-solid interaction is also a place where distorted elements may be found once regular mesh elements are cut by the solid boundary. The imposition of the boundary conditions on the immersed boundary is also a point of concern.

The IB method was first introduced by Peskin [1] and used source terms distributed through the solid region to indirectly enforce the proper boundary conditions on the solid-fluid interface. IB methods received particular attention in recent years. Their applications cover a broad spectrum of fluid dynamics problems from flow through heart devices [1, 2], to the interaction of body movement and fluid flow [3], modeling anguilliform swimming [4] and 3-D parachute simulation [5]. Reviews of IB methods may be found in [3] and [6]. Two classes of methods are discussed depending on how the source terms describing the presence of the boundary are imposed: directly in the continuous equations describing the flow (continuous forcing approach) or in the resulting system of linear equations (discrete forcing approach).

Most of the numerical developments were made in a finite difference framework and IB methods using finite elements were developed more recently. Glowinski *et al.* [7] proposed a Lagrange multiplier-based fictitious domain method which was further extended to obtain finite element solutions around moving rigid bodies using meshes which are not boundary fitted [8]. The method consists of filling the moving bodies by the surrounding fluid

and impose rigid body motions to the fluid occupying the regions originally occupied by the rigid bodies. The rigid body motion constraint is then relaxed by using distributed Lagrange multipliers and a flow problem over the entire domain is solved. A finite element implementation of the IB method which makes use of a Dirac function to impose the interaction force at the fluid-structure interface was presented by Boffi and Gastaldi [9]. A discussion on the stability of the space-time discretization can be found in [10]. Zhang *et al.* [11] present the immersed finite element method for the solution of fluid-structure interactions with deformable solids. In their method, a Lagrangian solid mesh moves on top of a background Eulerian fluid mesh which spans over the entire computational domain and a discretized delta function is used to describe the coupling between the fluid and solid domains. The finite element solution of the flow around immersed objects using a fixed mesh ALE approach is presented by Codina *et al.* [12]. In their work the solid boundary is represented using a level-set function defined on a background fixed mesh, while the moving boundary is treated by an ALE technique in the region close to the immersed surface. Boundary conditions on the immersed boundary are imposed by a least-squares approximation.

In most IB methods, boundary conditions on immersed surfaces are handled either accurately by using dynamic data structures to add/remove grid points as needed, or in an approximate way by imposing the boundary conditions to the grid point closest to the surface or through least-squares. Our recently proposed approach [13, 14] achieves the level of accuracy of cut cell dynamic node addition techniques with none of their drawbacks (increased CPU time and costly dynamic data structures). The finite element discretization of elements cut by the fluid/solid interface is enriched by the addition of degrees of freedom associated to interface nodes which are latter eliminated at element level. This approach is extended to fluid/solid interaction in the present contribution.

In this work the flow around immersed bodies is solved using a 3-D finite element IB method. The solution is interpolated using linear elements and time integration is done by an implicit Euler scheme. The immersed boundary is represented using a time dependent level-set function using the same linear interpolation functions that are used to solve the flow problem. Special emphasis is put on the computation of fluid/solid interaction forces. The proposed approach is verified on simple cases for which solutions on BC grids can be obtained and is then applied to more complex fluid/solid interaction problems.

The paper is organized as follows. The model problem and the associated finite element formulation is presented in section 2. The IB formulation is discussed briefly and the procedure to recover the forces acting on the solid surfaces is detailed. Section 3 illustrates the performance of the present IB method for a selection of 2-D and 3-D test problems. The paper ends with conclusions.

2. THE MODEL PROBLEM

We consider the transient incompressible fluid flow problem on a bounded computational domain Ω formed by the fluid region $\Omega_f(t)$ and the solid volume $\Omega_s(t)$ as shown in Figure 1. The fluid and solid volumes are time dependent but the total volume Ω formed by their reunion is not. The immersed interface $\Gamma_i(t) = \partial\Omega_f(t) \cap \partial\Omega_s(t)$ represents a boundary for the fluid flow and is considered as being time dependent.

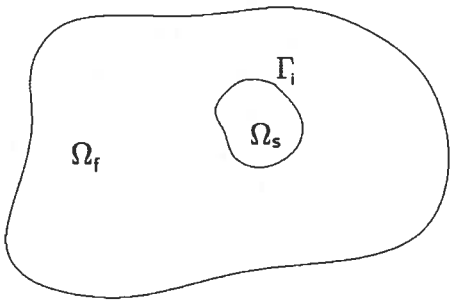

Figure 1: Computational domain formed by fluid region $\Omega_f(t)$ and solid region $\Omega_s(t)$.

2.1. Model equations and boundary conditions

The equations of motion are the incompressible Navier-Stokes equations:

$$\rho\left(\frac{\partial \mathbf{u}}{\partial t} + \mathbf{u}\cdot\nabla\mathbf{u}\right) = -\nabla p + \nabla\cdot\left[\mu\left(\nabla\mathbf{u} + (\nabla\mathbf{u})^T\right)\right] + \mathbf{f} \quad (1)$$

$$\nabla\cdot\mathbf{u} = 0, \quad (2)$$

where ρ is the density, $\mathbf{u}$ the velocity vector, p the pressure, μ the viscosity, and $\mathbf{f}$ a volumetric force vector.

The interface Γ_i, between the fluid and solid regions, is specified using a level-set function ψ, which is defined as a signed distance function from the immersed interface:

$$\psi(\mathbf{x},t) = \begin{cases} d(\mathbf{x},\mathbf{x}_i(t)), & \mathbf{x} \text{ in the fluid region,} \\ 0, & \mathbf{x} \text{ on the fluid/solid interface,} \\ -d(\mathbf{x},\mathbf{x}_i(t)), & \mathbf{x} \text{ in the solid region,} \end{cases} \tag{3}$$

where $d(\mathbf{x},\mathbf{x}_i(t))$ is the distance between the point $P(\mathbf{x})$ and the fluid/solid interface $P_i(\mathbf{x}_i(t))$ at time t. Hence, points in the fluid region have positive values of ψ, whereas points in the solid region have negative ones. The definition of the level-set function may be more complicated for complex 3-D geometries. In such a case, we may consider that the immersed boundary surface is provided in the form of a CAD file from which we generate a surface mesh with a mesh size sufficiently small to have a correct representation of the surface. Then, the level-set function is simply computed from the shortest distance between the nodes of the 3D mesh and the surface mesh. In this work only cases for which the level-set function is given analytically were considered.

The initial and boundary conditions associated to equations (1) and (2) are

$$\mathbf{u} = \mathbf{U}_0(\mathbf{x}), \qquad \text{for } t = t_0, \tag{4}$$

$$\mathbf{u} = \mathbf{U}_D(\mathbf{x},t), \qquad \text{for } \mathbf{x} \in \Gamma_D(t), \tag{5}$$

$$\mu\left(\nabla\mathbf{u} + \nabla\mathbf{u}^T\right)\cdot\hat{\mathbf{n}} - p\hat{\mathbf{n}} = \mathbf{t}(\mathbf{x},t), \qquad \text{for } \mathbf{x} \in \Gamma_t(t), \tag{6}$$

where Γ_D is the portion of the fluid boundary $\partial\Omega_f$ where Dirichlet conditions are imposed, and $\mathbf{t}$ is the traction imposed on the remaining fluid boundary $\Gamma_t = \partial\Omega_f \backslash \Gamma_D$. Dirichlet boundary conditions are imposed at the interface between fluid and solid regions, i.e. $\Gamma_i \subset \Gamma_D$. Because Γ_i is not represented by the finite element discretization, a special procedure is used to enforce velocity boundary conditions on this surface. This approach will be discussed in Section 2.3.

2.2. The Finite Element Formulation

The finite element formulation is the same as in reference [14]. Time derivatives are computed using an implicit Euler scheme. Both velocity and pressure are discretized using linear continuous interpolants and the

weak form of the equations corresponds to the GLS (Galerkin Least-Squares) method:

$$\int_\Omega \rho\left(\frac{\mathbf{u}-\mathbf{u}_0}{\Delta t}+\mathbf{u}\cdot\nabla\mathbf{u}\right)N_i^u \mathrm{d}\Omega - \int_\Omega p\nabla N_i^u \mathrm{d}\Omega + \int_\Omega \mu\left(\nabla\mathbf{u}+\nabla\mathbf{u}^T\right)\cdot\nabla N_i^u \mathrm{d}\Omega - \int_\Omega \mathbf{f}N_i^u \mathrm{d}\Omega + \sum_K \int_{\Omega_K}\left\{\rho\left(\frac{\mathbf{u}-\mathbf{u}_0}{\Delta t}+\mathbf{u}\cdot\nabla\mathbf{u}\right)+\nabla p - \nabla\cdot\left[\mu\left(\nabla\mathbf{u}+\nabla\mathbf{u}^T\right)\right]-\mathbf{f}\right\}\tau_u\mathbf{u}\cdot\nabla N_i^u \mathrm{d}\Omega_K = \int_{\Gamma_t}\mathbf{t}N_i^u \mathrm{d}\Gamma, \quad (7)$$

$$\int_\Omega \nabla\cdot\mathbf{u}N_i^p \mathrm{d}\Omega + \sum_K \int_{\Omega_K}\left\{\rho\left(\frac{\mathbf{u}-\mathbf{u}_0}{\Delta t}+\mathbf{u}\cdot\nabla\mathbf{u}\right)+\nabla p - \nabla\cdot\left[\mu\left(\nabla\mathbf{u}+\nabla\mathbf{u}^T\right)\right]-\mathbf{f}\right\}\tau_p\nabla N_i^p \mathrm{d}\Omega_K = 0, \quad (8)$$

where $(\mathbf{u}, p)$ is the solution at the current time step t_n, $\mathbf{u}_0$ is the solution at the previous time step t_{n-1} and $\Delta t = t_n - t_{n-1}$ is the time step increment. N_i^u, N_i^p are continuous, piecewise linear test functions associated to the velocity and pressure equations. The first four integrals in the right hand side of equation (7) and the first integral in equation (8) correspond to the Galerkin formulation whereas the integrals over the elements interior are the GLS stabilization terms. The stabilization parameters are computed as from Refs. [15, 16]:

$$\tau_u = \tau_p = \left[\left(\frac{2\rho|\mathbf{a}|}{h_K}\right)^2 + \left(\frac{4\mu}{m_k h_K^2}\right)^2\right]^{-1/2} \quad (9)$$

Here h_K is the size of the element K and m_k is a coefficient set to $1/3$ for linear elements (see [15, 17]).

The nonlinear equations for the velocity and pressure, are solved with a few Picard steps followed by Newton-Raphson iterations. The resulting linear systems are generated directly in a compressed sparse row format [18], and solved using the bi-conjugate gradient stabilized (Bi-CGSTAB) iterative method [19] with an ILU preconditioner.

2.3. The IB method

The algorithm used to treat the immersed boundary surface is the same as introduced by Ilinca and Hétu for the static fluid/solid interfaces [13] and

for moving interfaces [14].

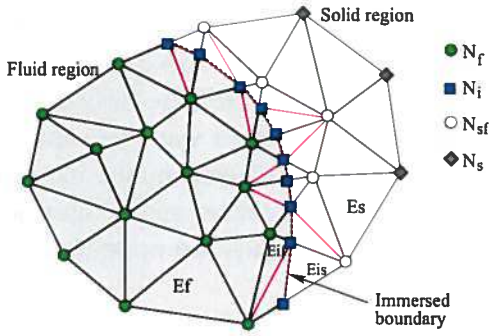

Figure 2: Decomposition of elements cut by the immersed boundary.

The mesh is intersected by the interface at the current time step t_n at points located along element edges (N_i in Figure 2) and we consider those points as additional degrees of freedom in the finite element formulation. While elements cut by the immersed boundary have nodes in both fluid and solid regions, the addition of nodes on the interface and the decomposition of interface elements yields the formation of elements which are either entirely in the fluid region (E_{if} in Figure 2) or in the solid region (E_{is} in Figure 2).

When solving the fluid flow we consider that the solid embedded in the mesh has a prescribed velocity $\mathbf{u_s(t)}$. This velocity can also be computed from the forces applied on the solid body. The solid velocity is therefore imposed on the solid nodes including the additional interface nodes. By doing so no additional degrees of freedom need to be included for the interface nodes. Only the right hand side of equations associated to fluid nodes connected to them will change and by these means take into account the location of the interface.

The pressure degrees of freedom are associated to the continuity equations. In order to enforce mass conservation in the entire fluid region, the continuity equations are solved on all fluid elements, including the fluid subelements at the interface. The continuity equations are not solved in the solid elements and the pressure is set to a constant (say zero) on solid nodes. The pressure discretization is considered discontinuous between interface subelements and the additional pressure degrees of freedom corresponding to interface nodes are eliminated by static condensation. For more details the reader should consult [13, 14].

The use of a discontinuous pressure interpolation for interface sub-elements introduces more freedom to the finite element space. The advantage of such an approach is that the additional pressure degrees of freedom at the interface nodes can be eliminated locally on each sub-element. One major drawback however is that the resulting pressure will be discontinuous at the interface nodes, while the actual pressure field we want to solve is continuous. In order to increase the regularity of the discontinuous interface pressure we have opted for a modified pressure stabilization inside interface sub-elements. For sub-elements containing interface nodes the pressure stabilization parameter in equation (8) was taken

$$\tau_p^* = 6\tau_p \tag{10}$$

It means that the pressure stabilization is increased only for interface sub-elements containing the discontinuous pressure discretization. Numerical tests indicated that the factor 6 is quite optimal as a closer to continuous interface pressure is obtained without introducing undesired diffusion.

2.4. Computation of fluid/solid interaction forces

In this work the fluid and solid equations are solved separately. The fluid flow uses the solid velocity as boundary conditions and then provides the forces acting on the solid to serve in the computation of the solid body movement. One main aspect in the simulation of fluid/solid interaction is therefore the computation of the interaction forces between the fluid and solid. The force acting on the fluid at the solid interface is computed from:

$$\mathbf{F}_F(t) = \int_{\Gamma_i} \left[\mu \left(\nabla \mathbf{u} + \nabla \mathbf{u}^T\right) \cdot \hat{\mathbf{n}} - p\hat{\mathbf{n}}\right] \mathrm{d}\Gamma, \tag{11}$$

where the fluid/solid interface Γ_i is considered as formed by the triangular faces of interface sub-elements having all three nodes on the interface and $\hat{\mathbf{n}}$ is the outward unit normal vector on these faces. Remark that while the pressure and the unit normal vector are computed for each triangular face from the values at the vertices of the face, the velocity gradient is a quantity which should be recovered from the three-dimensional tetrahedral interface sub-element containing the respective face. Integration is however simplified by the fact that the velocity gradient is a constant piecewise quantity, whereas the pressure is linear.

The force acting on the solid may be seen as a reaction force and has the same magnitude as the force on the fluid but acts in the opposite direction:

$$\mathbf{F}_S = -\mathbf{F}_F \tag{12}$$

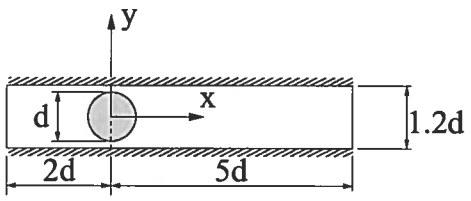

Figure 3: Computational domain for flow in a channel obstructed by a cylinder.

As it is the case very often in aero and hydrodynamic applications, in the work shown in the next section we will make reference to the drag and lift coefficients acting on the solid immersed body. These are dimensionless coefficients representing the normalized forces acting in streamline direction for the drag and normal to the streamline direction for the lift and are determined as:

$$C_D = \frac{\mathbf{F}_{Sx}}{\frac{1}{2}\rho U_0^2 A} \tag{13}$$

$$C_L = \frac{\mathbf{F}_{Sy}}{\frac{1}{2}\rho U_0^2 A} \tag{14}$$

where ρ is the fluid density, U_0 is a velocity scale representative of the flow field and A is a representative area of the body. Usually for a sphere of diameter d we have $A = \pi d^2/4$ and for a cylinder of diameter d and length L placed along a direction normal to the flow we have $A = dL$.

3. APPLICATIONS

3.1. Flow inside a channel obstructed by a cylinder

This first validation test consists in the 2-D flow in a channel obstructed by a cylinder placed at equal distance from the channel walls as shown in Figure 3. The flow enters the domain from the left at uniform speed U_0 and the obstruction ratio is $1 : 1.2$. Because the problem is two-dimensional, only a slab of thickness $0.2d$ was meshed with 3D tetrahedral elements and the w component of the velocity was set to zero. The mesh was generated for both the fluid region and the interior of the cylinder. In such a way the problem can be solved by the IB method considering the entire computational domain and also by a standard method on a body-conforming (BC) mesh representing only the fluid region. This will result in a rigorous evaluation of the

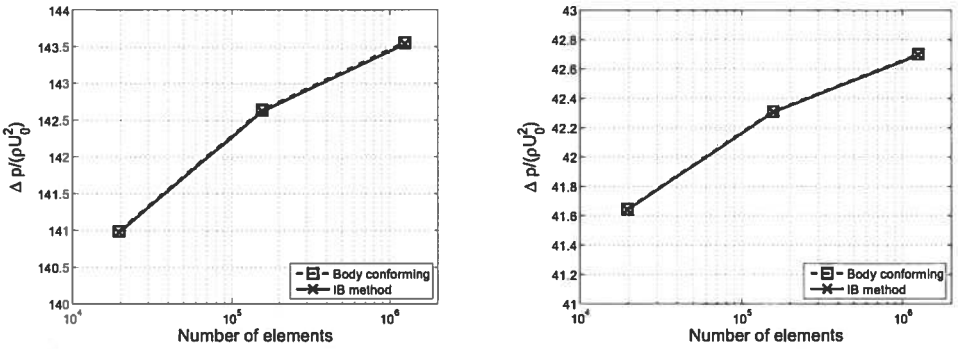

(a) $Re = 20$ (b) $Re = 80$

Figure 4: Pressure drop determined by the cylinder obstruction

performance of the IB method since the IB and BC solutions are obtained on similar meshes. The solid interface in the IB method is determined by the level-set function $\psi = r - R$, where $r = (x^2 + y^2)^{1/2}$ is the distance from the point $P(x, y)$ to the center of the cylinder and R is the cylinder radius. Therefore, IB simulations can be carried out for different values of the cylinder radius by simply modifying the level-set function to the corresponding value of R.

Simulations were carried out for two flow regimes: low Reynolds number $Re = \rho U_0 d/\mu = 20$ and moderate Reynolds number $Re = \rho U_0 d/\mu = 80$. In both cases a steady state solution is obtained. The pressure drop along the channel generated by the presence of the cylinder as computed by the IB and BC methods is compared in Figure 4 for three meshes with different mesh refinement. The coarser mesh, Mesh 1, has 19,520 tetrahedral elements and two successively refined meshes are obtained by reducing in half the element size, thus resulting in an eight fold increase in the number of elements after each refinement. Mesh 2 has 156,160 elements and Mesh 3 has 1,249,280 elements. As can be seen, the pressure drop provided by the IB method is virtually the same as the one computed on a BC mesh for all three meshes.

The force acting on the cylinder is plotted in Figure 5. Solutions were obtained by the IB method for different values of the cylinder radius R ranging between $0.99R_0$ and $1.01R_0$, with $R_0 = d/2$ being the reference value of the radius used in the BC solution. The lines in Figure 5 indicate the dependence of the drag coefficient on the cylinder radius as computed by

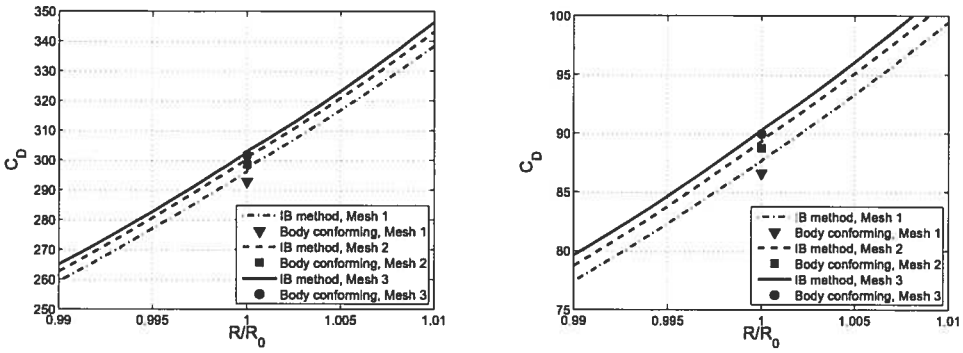

(a) $Re = 20$ (b) $Re = 80$

Figure 5: Drag coefficient on the cylinder

the IB method and the symbols indicate the corresponding drag coefficient from the BC solution which is available only for $R = R_0$. Remark that for all three meshes the IB and BC solutions compare extremely well. The IB solutions for various cylinder radius were computed by using increments as small as $10^{-4}R_0$, thus indicating that the method is sensitive even to such a small change in the position of the solid-fluid interface. Recall that all three meshes have been generated in such a way as to have mesh nodes on the interface only for $R = R_0$. In all cases the solution exhibits smooth changes when the cylinder radius varies from smaller than R_0 to larger than R_0 values and the method is stable and accurate even when very small interface elements are generated as is the case when R is very close to R_0.

3.2. Steady cylinder in uniform flow

This problem consists in the flow around a stationary circular cylinder placed in uniform flow. The computational domain and boundary conditions are shown in Figure 6 with the flow entering the left side with uniform velocity. The cylinder is located at 10 diameters from the inlet and at 24 diameters from the outlet. The height of the computational domain is $35d$ thus corresponding to an obstruction ratio $\lambda = 0.0286$. Because the problem is two-dimensional, only a slab was meshed with 3D tetrahedral elements and the w component of the velocity was set to zero. The mesh was designed to have smaller elements in the region of the immersed cylinder and in the wake of the cylinder where the solution is expected to exhibit larger time variations. The grid has 376 elements in flow direction, 176 elements in direction

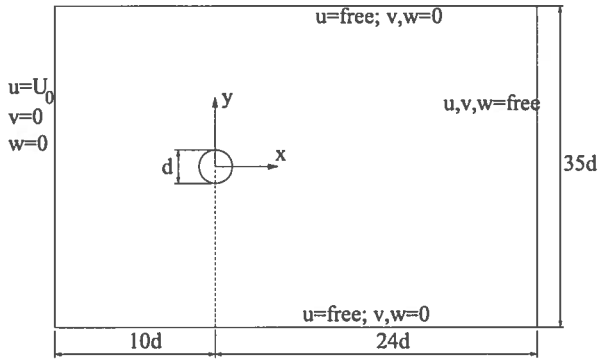

Figure 6: Uniform flow around a circular cylinder: Domain and boundary conditions.

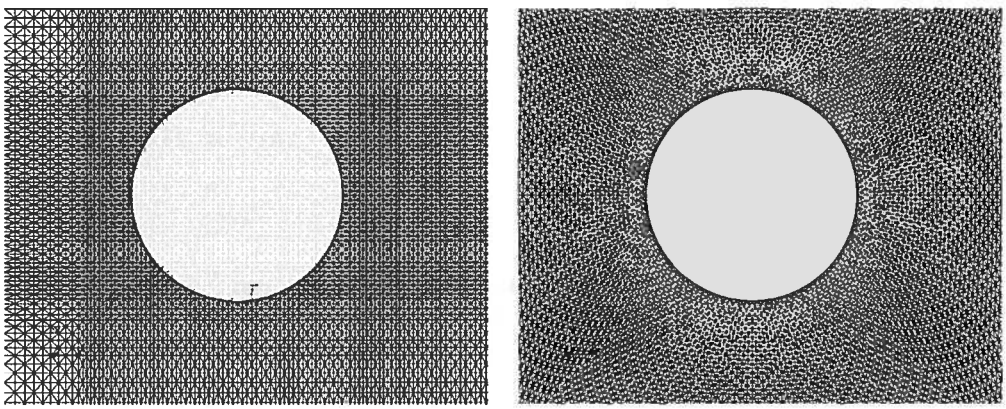

(a) IB mesh (b) Body conforming mesh

Figure 7: Mesh for the flow around a circular cylinder

normal to the flow and only 2 elements are used in the width of the slab for a total of 661,760 tetrahedral elements. A detail of the mesh in the region of the cylinder is shown in Figure 7(a). The part of the mesh contained inside the solid cylinder is plotted with a lighter gray color to indicate that only the solution in the fluid region is computed. To quantify the accuracy of the IB solution, comparison was made with the finite element solution computed on a BC grid with similar mesh size as shown in Figure 7(b). The BC grid has 665,600 tetrahedral elements.

Table 1: Steady flow past a circular cylinder: length L of standing eddy behind the cylinder and drag coefficient C_D.

	L	C_D
$Re = 20$		
Linnick and Fasel [20], $\lambda = 0.056$	0.93	2.16
Linnick and Fasel [20], $\lambda = 0.023$	0.93	2.06
Present, BC, $\lambda = 0.0286$	0.947	2.188
Present, IB, $\lambda = 0.0286$	0.948	2.127
$Re = 40$		
Linnick and Fasel [20], $\lambda = 0.056$	2.23	1.61
Linnick and Fasel [20], $\lambda = 0.023$	2.28	1.54
Cheny and Botella [21]	2.299	1.508
Present, BC, $\lambda = 0.0286$	2.294	1.613
Present, IB, $\lambda = 0.0286$	2.298	1.580

This problem was the object of several numerical studies. It was used as a test problem for the immersed boundary methods proposed by Linnick and Fasel [20] and by Cheny and Botella [21]. It has also been used by the authors to validate the behavior of the proposed IB method [13]. However, while in reference [13] only the flow response was analyzed, the present work emphasizes on the fluid-solid interaction force. Present computations were carried out for Reynolds numbers $Re = \rho U_0 d/\mu$ ranging from 20 to 200. The critical Reynolds number for this flow is $Re_{cr} = 51$ [22]. For flows having Reynolds numbers smaller than Re_{cr} we expect to obtain a steady state solution presenting two symmetrically located standing eddies behind the cylinder. For higher Reynolds numbers than Re_{cr} the flow becomes unsteady and the well known Karman vortex street forms in the wake of the cylinder.

Table 2: Unsteady flow past a circular cylinder: Strouhal number St, drag coefficient C_D, and lift coefficient C_L.

	St	C_D	C_L
$Re = 100$			
Liu *et al.*[23]	0.165	1.35 ± 0.012	± 0.339
Linnick and Fasel [20], $\lambda = 0.056$	0.169	1.38 ± 0.010	± 0.337
Linnick and Fasel [20], $\lambda = 0.023$	0.166	1.34 ± 0.009	± 0.333
Cheny and Botella [21]	0.170	1.317 ± 0.009	-
Present, BC, $\lambda = 0.0286$	0.1679	1.369 ± 0.0087	± 0.323
Present, IB, $\lambda = 0.0286$	0.1679	1.360 ± 0.0092	± 0.324
$Re = 200$			
Belov *et al.* [24]	0.193	1.19 ± 0.042	± 0.64
Liu *et al.* [23]	0.192	1.31 ± 0.049	± 0.69
Linnick and Fasel [20], $\lambda = 0.056$	0.199	1.37 ± 0.046	± 0.70
Linnick and Fasel [20], $\lambda = 0.023$	0.197	1.34 ± 0.044	± 0.69
Cheny and Botella [21]	0.200	1.327 ± 0.045	-
Present, BC, $\lambda = 0.0286$	0.1989	1.343 ± 0.0428	± 0.670
Present, IB, $\lambda = 0.0286$	0.1989	1.349 ± 0.0447	± 0.677

The IB results are compared with the solutions on the BC mesh as well as with other numerical solutions in Table 1 for $Re = 20$ and $Re = 40$, and in Table 2 for $Re = 100$ and $Re = 200$. The present BC and IB predictions of the mean drag coefficient and of the maximum lift coefficient are compared in Figure 8. For the steady state cases the IB method recovers almost the same length of the recirculation region behind the cylinder and shows a 2-3% difference for the drag coefficient when compared with the BC solutions. For the higher Reynolds number flows the vortex shedding frequency is virtually the same for the IB and BC solutions, while the drag and lift coefficients show differences smaller than 1%.

3.3. In-line oscillating cylinder in uniform flow

For this test problem an in-line oscillating cylinder is placed in uniform flow. The computational domain and boundary conditions are the same as for the stationary cylinder case of section 3.2. Here again the accuracy of the IB solution is verified with respect to the finite element solution computed

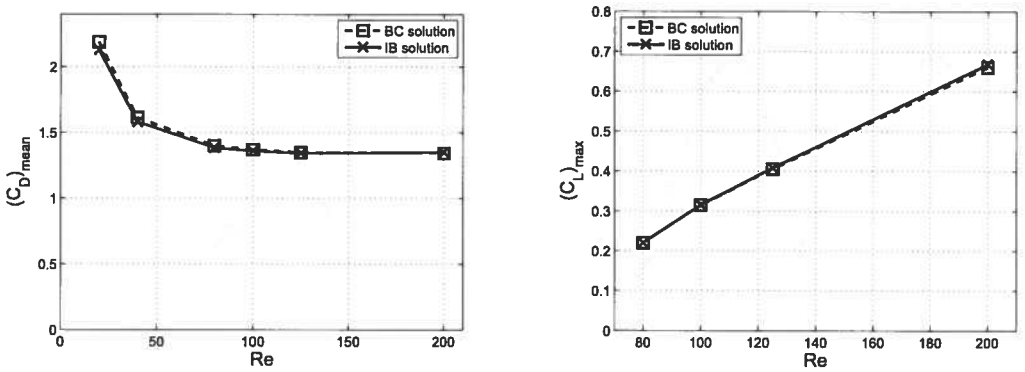

(a) Mean drag coefficient

(b) Maximum lift coefficient

Figure 8: Dependence of the drag and lift coefficients with respect to the Reynolds number.

on the BC grid. Because the position of the cylinder changes with time we use for the BC mesh an Arbitrary Lagrangian-Eulerian formulation on a deforming mesh as described in [14]. Mesh deformation parameters are the same as those of Ilinca and Hétu [14].

Numerical simulations were conducted using the flow parameters of Saiki and Biringen [25]. The Reynolds number is $Re = \rho U_0 d/\mu = 200$, where U_0 is the free-stream velocity and d is the cylinder diameter. The cylinder is oscillating parallel to the free-stream flow at a frequency $f_c = 1.88 f_s$, with f_s being the Strouhal frequency for the stationary cylinder. For $Re = 200$ we have $St = f_s d/U_0 = 0.1989$ (see Table 2) and therefore $f_c = 0.374 U_0/d$. The center of the cylinder is considered initially at $x_c = 0$, $y_c = 0$ and is displaced in time following the relationship $x_c = A_c sin(2\pi f_c t)$ with $A_c = 0.24$. Experimental data for the same conditions and $Re = 190$ are reported by Griffin and Ramberg [26] and similar experiments were made by Ongoren and Rockwell [27]. It is reported that there are three vortices shed during a cycle of the motion, two being clockwise and one counter-clockwise. This flow pattern is identified as anti-symmetrical mode A-III by Ongoren and Rockwell [27] and occurs when f_c/f_s is close to 2. Numerical solutions using an IB method for $Re = 100$ and $f_c/f_s = 2$ are provided by Liao *et al.* [28].

Following the work of Sohankar [22], the time-step was initially set to $\Delta t = 0.025 d/U_0$. Simulations were also performed with smaller time steps, $\Delta t = 0.0125 d/U_0$, $\Delta t = 0.00625 d/U_0$ and $\Delta t = 0.003125 d/U_0$ respectively. It was found that differences between the solutions for the two smallest time

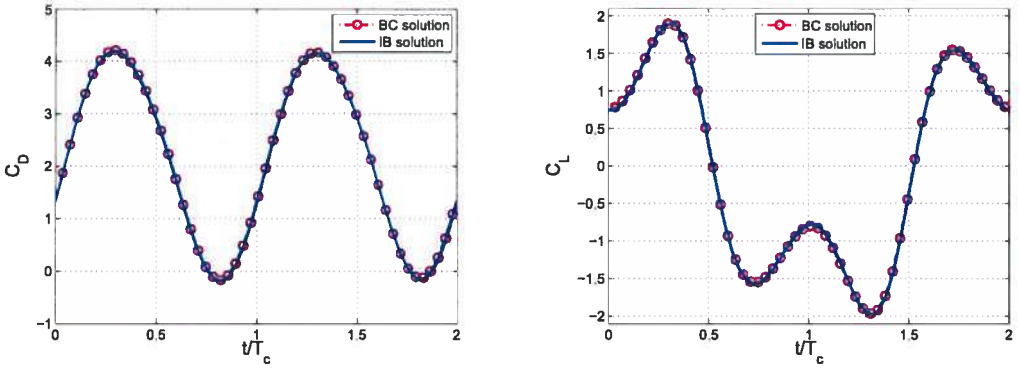

(a) Drag coefficient

(b) Lift coefficient

Figure 9: Drag and lift coefficients for anti-symmetrical mode A-II.

steps were negligible and therefore we present here only the results for $\Delta t = 0.00625 d/U_0$. Both the IB and BC-ALE solutions resulted in a periodic flow with a time period twice that of the oscillating cylinder ($T = 2T_c$) in agreement with the experimental observations.

Numerical simulations carried out with both BC and IB methods indicate that the flow exhibits first an anti-symmetrical mode A-II as of Ongoren and Rockwell [27] in which two vortices shed during a flow period, one clockwise and the other counter-clockwise. During this initial period of time the drag and lift coefficients varies as shown in Figure 9. The drag coefficient has the same period of oscillation as the movement imposed on the cylinder T_c because the drag is the same when vortices shed from the upper or the lower part of the cylinder. The lift coefficient has a period twice that of the cylinder with the values taken in the second cylinder period equal in amplitude but with opposite sign than those taken in the first cylinder oscillation period. This flow pattern is however unstable and the flow rapidly evolves toward an anti-symmetrical mode A-III as of Ongoren and Rockwell [27]. The drag and lift coefficient for this type of flow pattern are shown in Figure 10.

Vorticity contours during a vortex shedding period for the stable A-III flow pattern are shown in Figure 11. Results indicate that the two methods produce very similar solutions, thus indicating that the IB method performs well. Recall that the time period of vortex shedding T is twice that of the cylinder oscillation T_c. Three vortices shed during a cycle of the motion (composed of two complete oscillations of the cylinder), two being clockwise

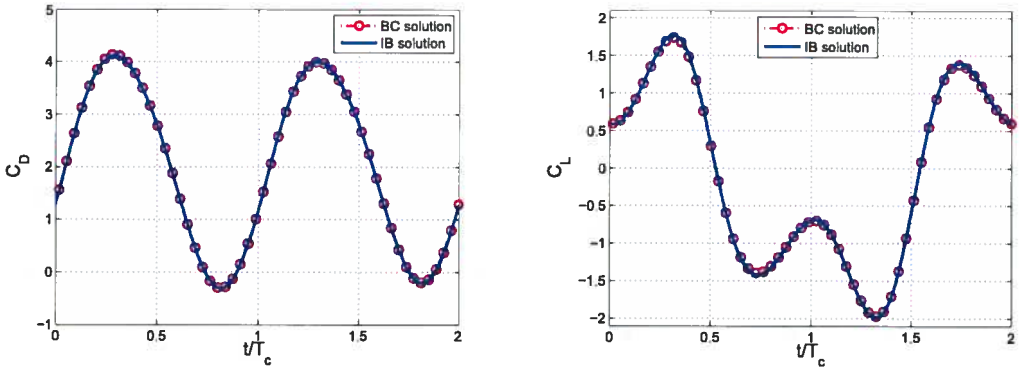

(a) Drag coefficient

(b) Lift coefficient

Figure 10: Drag and lift coefficients for anti-symmetrical mode A-III.

(red in Figure 11) and one counter-clockwise (blue in Figure 11).

3.4. Sphere settling under gravity

A 3-D fluid-solid interaction problem for which experimental data are available is the falling of a sphere under gravity in an enclosure filled with a viscous fluid. In the experimental setup of ten Cate *et al.* [29] the sphere has a diameter $d = 0.015m$ and is placed inside a box of dimensions $0.1 \times 0.1 \times 0.16m^3$ as shown in Figure 12(a). The sphere is released at a initial height of $0.12m$ from the bottom of the box. The present IB method was tested for the same set of conditions used in the experiment of ten Cate *et al.* [29] and for which numerical results given by an immersed boundary method were presented by Liao *et al.* [28]. The density of the falling sphere is $\rho_s = 1120kg/m^3$ and the fluid properties for the four cases considered are summarized in Table 3.

Table 3: Fluid properties for sphere settling under gravity.

Case	Re	$\rho(kg/m^3)$	$\mu(Ns/m^3)$
E1	1.5	970	0.373
E2	4.1	965	0.212
E3	11.6	962	0.113
E4	31.9	960	0.058

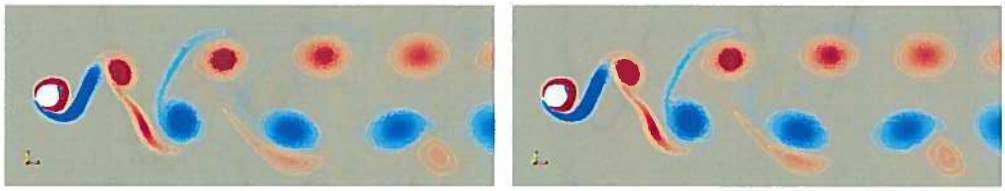

(a) $t = 2nT_c$; IB method

(b) $t = 2nT_c$; BC-ALE

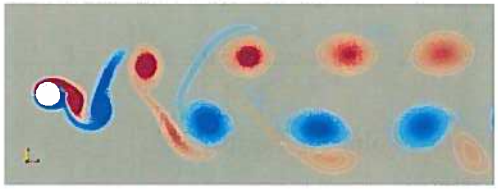

(c) $t = 2nT_c + T_c/2$; IB method

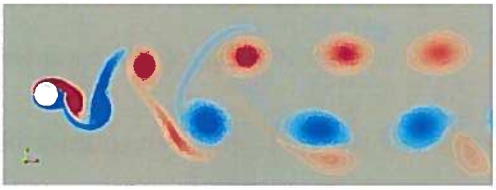

(d) $t = 2nT_c + T_c/2$; BC-ALE

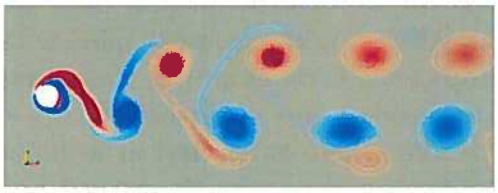

(e) $t = 2nT_c + T_c$; IB method

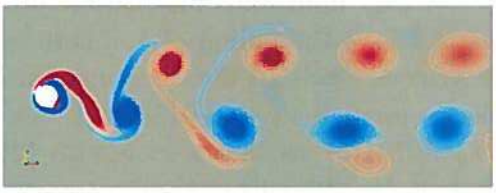

(f) $t = 2nT_c + T_c$; BC-ALE

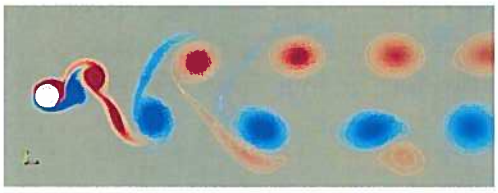

(g) $t = 2nT_c + 3T_c/2$; IB method

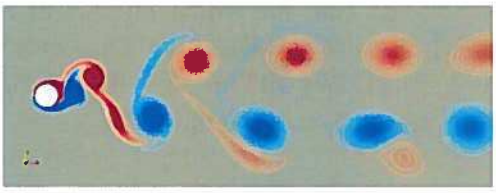

(h) $t = 2nT_c + 3T_c/2$; BC-ALE

Figure 11: Vorticity contours: Comparison of IB (left) and BC-ALE (right) solutions.

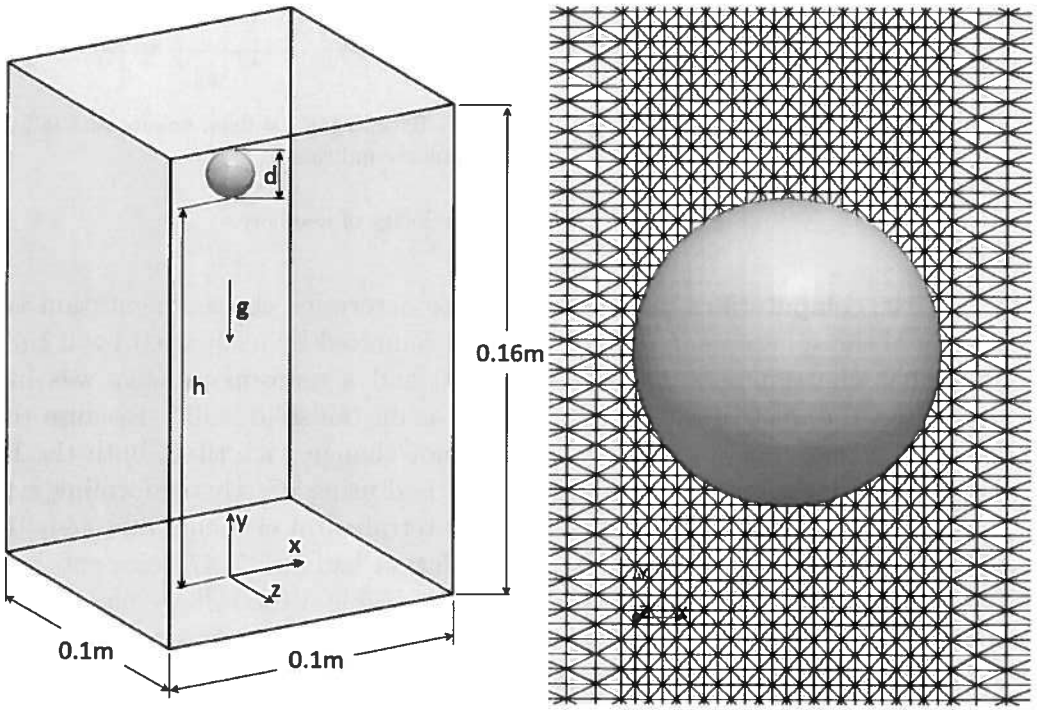

(a) Computational domain (b) Detail of the mesh

Figure 12: Computational domain and mesh for the falling sphere.

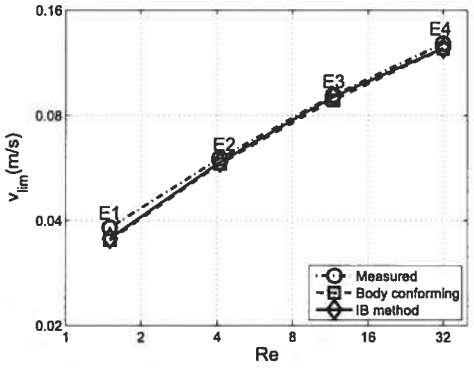

(a) Fixed sphere in uniform flow

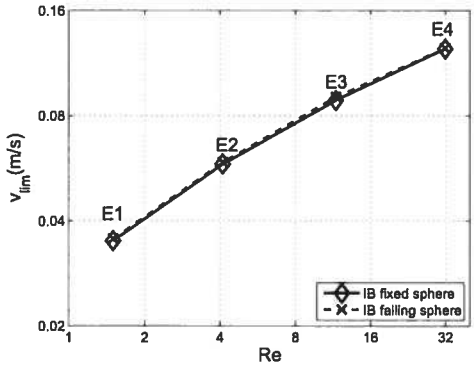

(b) IB solution for fixed sphere and falling sphere conditions

Figure 13: Sedimentation velocity of a sphere.

First, computations were carried out to determine the sedimentation velocity of the sphere in an infinite medium delimited by a square $0.1 \times 0.1m^2$. For this, the sphere was considered fixed and a uniform velocity was imposed on the inlet of the domain as well as on the solid walls. Because the computational domain in this case does not change with time, both the IB method and a standard finite element method using a body conforming grid were used. The BC mesh had $2,869,849$ tetrahedral elements and $484,714$ nodes, whereas the mesh for the IB simulation had $3,147,473$ elements and $533,022$ nodes. For each one of the cases of Table 3 the inflow velocity was varied until the drag force on the sphere was equal to the gravity force, thus obtaining the sedimentation velocity. The resulting sedimentation velocity is compared with the velocity determined by ten Cate *et al.* [29] in Figure 13(a). As can be seen, the present finite element solutions for BC and IB conditions results in almost the same sedimentation velocity. The agreement with the measured values is also excellent, except for the smallest Reynolds number case. For $Re = 1.5$ the difference between the computed and measured sedimentation velocity is however less than 5% thus remaining in the accuracy limits of the experimental setup.

The IB method was then used to determine the movement of the falling sphere inside the rectangular enclosure until it reaches the bottom wall. The mesh used for this simulation has $2,545,928$ elements and $533,022$ node. A detail of the mesh in near the sphere is shown in Figure 12(b). The maxi-

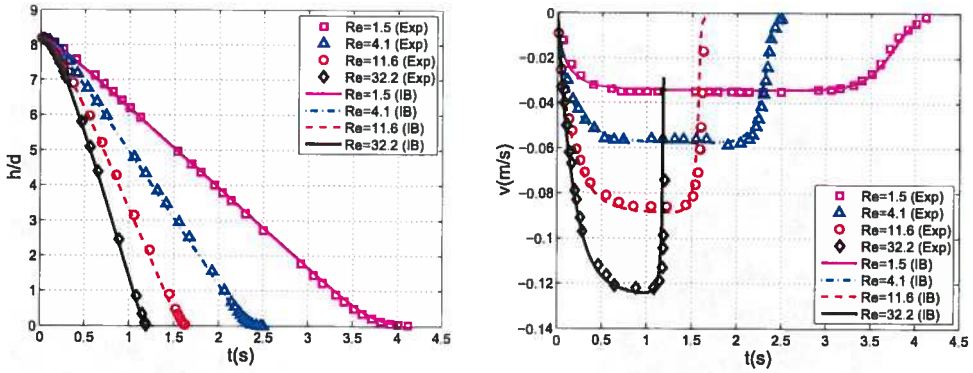

(a) Height relative to the bottom wall

(b) Velocity

Figure 14: Evolution with time of the position and velocity of the sphere.

mum settling velocity reached for the four test cases is compared in Figure 13(b) with the sedimentation velocity computed previously by considering the sphere as being fixed. The IB method applied to the falling sphere case produces almost the same sedimentation velocity as the one obtained considering the fixed sphere placed in an uniform flow. This indicates that the IB method applied on the moving fluid/solid interface performs well.

The evolution with time of the sphere position and velocity is compared with the measured values of ten Cate *et al.* [29] in Figure 14. In the experiment it is indicated that the sphere is released at an initial height of $0.12m$ which is eight times the diameter of the sphere. However, by integrating the measured velocities we obtain that the actual initial position of the sphere is close to $0.123m$ or 8.2 times the sphere diameter. This difference may be determined by the procedure to release the sphere in the experimental setup. Therefore we considered that the sphere is released at $h = 8.2d$ instead of $h = 8d$. This modification does not affect the velocity of the sphere except for the very last part of the falling trajectory, but results in a better consistency with the measured position. The results indicate an excellent agreement with the measured data for all cases considered. Without the above mentioned correction the sphere would have reached the bottom wall faster than in the experiment for $Re = 1.5$ even if the computed velocity is slightly smaller than measured.

Figure 15 shows the position of the falling sphere at various times as well as the velocity distribution in a section across the sphere center for the case

(a) $t = 0$

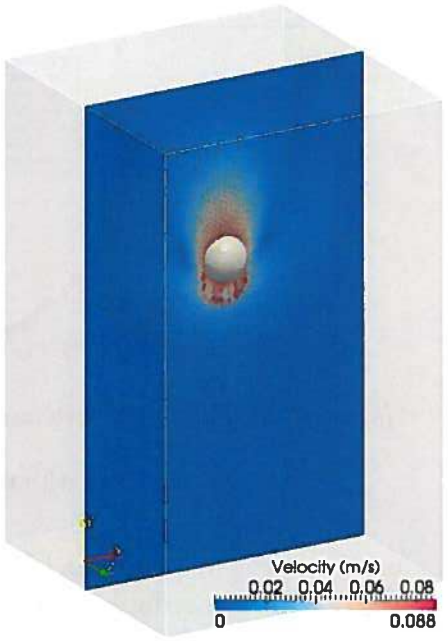

(b) $t = 0.5s$

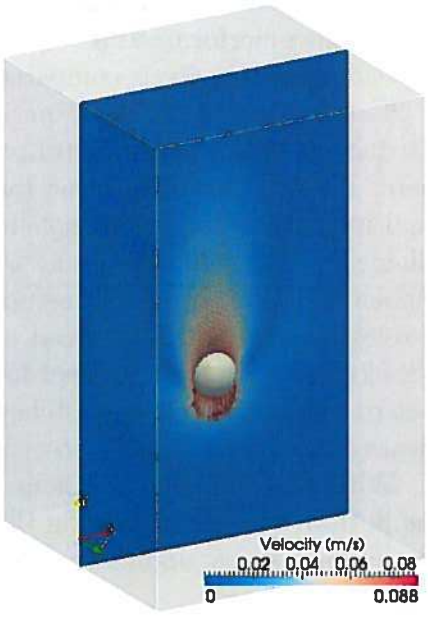

(c) $t = 1.0s$

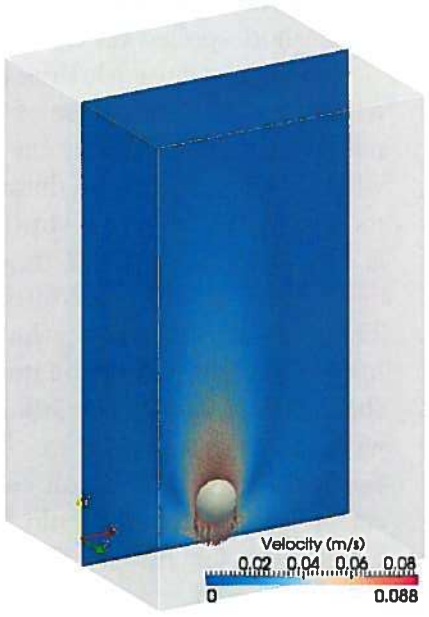

(d) $t = 1.5s$

Figure 15: Sphere falling for the conditions of case $E3$.

$E3$. At $t = 0$ (Figure 15(c)) the sphere is standing still and there is no flow around it. Once the sphere is released, it accelerates gradually and the fluid flow in the box evolves accordingly. At $t = 1.0s$ the sphere almost reached the maximum sedimentation velocity and then at $t = 1.5s$ the deceleration caused by the proximity of the bottom wall has started as confirmed by the results presented in Figure 14.

4. CONCLUSIONS

An accurate IB finite element method for computing the fluid/solid interaction forces is presented. The boundary conditions are imposed on the immersed interface by incorporating into the grid the points where the mesh intersects the fluid/solid boundary. The degrees of freedom associated with the additional grid points are eliminated either because the velocity is known or by static condensation in the case of the pressure. The velocity and pressure solution on interface sub-elements are then used to determine the forces acting on the solid surface.

Application of the proposed method to the flow in an obstructed channel shows an excellent agreement with body-conforming grid solutions. The agreement improves when the mesh is refined. The IB method applied for different values of the obstruction size (cylinder diameter) shows the ability of the method to accurately tackle very small changes in solid shape and dimensions and to deal with very small or distorted elements.

For the flow around a steady cylinder the IB and BC methods provide results very close to each other. The computed forces acting on the cylinder are in good agreement with previous numerical results for both steady-state and transient periodic flows.

For the application to transient flow past a circular cylinder oscillating in-line with the free-stream the results compare well with experimental data and with numerical results on body-conforming mesh. The IB solution develops first an anti-symmetric A-II flow pattern which is unstable, thus evolving into the A-III flow pattern. This anti-symmetric vortex shedding was observed experimentally for a frequency of the cylinder oscillation near twice that of the vortex shedding behind the stationary cylinder.

The three-dimensional IB finite element method was also used to solve the settling of a single sphere in a viscous fluid. The IB solution is accurate as the resulting sedimentation velocity is close to the measured value. Simulations

for different flow regimes indicate an excellent agreement with the experiment for both the position and velocity of the sphere.

REFERENCES

[1] C.S. Peskin, "Flow patterns around heart valves: a numerical method," *Journal of Computational Physics*, vol. 10, pp. 252–271, 1972.

[2] C.S. Peskin, "Numerical analysis of blood flow in the heart," *Journal of Computational Physics*, vol. 25, pp. 220–252, 1977.

[3] R. Mittal and G. Iaccarino, "Immersed boundary methods," *Annu. Rev. Fluid Mech.*, vol. 37, pp. 239–261, 2005.

[4] R. Tyson, C.E. Jordan and J. Hebert, "Modelling anguilliform swimming at intermediate Reynolds number: A review and a novel extension of immersed boundary method applications," *Comput. Methods Appl. Mech. Engrg.*, vol. 197, pp. 2105–2118, 2008.

[5] Y. Kim and C.S. Peskin, "3-D parachute simulation by the immersed boundary method," *Computers & Fluids*, vol. 38, pp. 1080–1090, 2009.

[6] F. Margnat and V. Morinière, "Behaviour of an immersed boundary method in unsteady flows over sharp-edged bodies," *Computers & Fluids*, vol. 38, pp. 1065–1079, 2009.

[7] R. Glowinski, T.-W. Pan and J. Périaux, "A fictitious domain method for external incompressible viscous flow modeled by Navier-Stokes equations," *Comput. Methods Appl. Mech. Engrg.*, vol. 112, pp. 133–148, 1994.

[8] R. Glowinski, T.-W. Pan, T.I. Hesla, D.D. Joseph and J. Périaux, "A distributed Lagrange multiplier/fictitious domain method for flows around moving rigid bodies: application to particulate flows," *International Journal for Numerical methods in Fluids*, vol. 30, pp. 1043–1066, 1999.

[9] D. Boffi and L. Gastaldi, "A finite element approach for the immersed boundary method," *Computers and Structures*, vol. 81, pp. 491–501, 2003.

[10] D. Boffi, L. Gastaldi and L. Heltai, "On the CFL condition for the finite element immersed boundary method," *Computers and Structures*, vol. 85, pp. 775–783, 2007.

[11] L. Zhang, A. Gerstenberger, X. Wang and W.K. Liu, "Immersed finite element method," *Comput. Methods Appl. Mech. Engrg.*, vol. 193, pp. 2051–2067, 2004.

[12] R. Codina, G. Houzeaux, H. Coppola-Owen and J. Baiges, "The fixed mesh ALE approach for the numerical approximation of flows in moving domains," *Journal of Computational Physics*, vol. 228, pp. 1591–1611, 2009.

[13] F. Ilinca, J.-F. Hétu, "A finite element immersed boundary method for fluid flow around rigid objects," *Int. Journal for Numerical Methods in Fluids*, 2010, in press. doi:10.1002/fld.2222.

[14] F. Ilinca, and J.-F. Hétu, "A finite element immersed boundary method for fluid flow around moving objects," *Computers and Fluids*, vol. 39, pp. 1656–1671, 2010.

[15] T.E. Tezduyar, R. Shih, S. Mittal and S.E. Ray, "Incompressible flow using stabilized bilinear and linear equal-order-interpolation velocity-pressure elements," *Research Report UMSI 90/165*, University of Minnesota/Supercomputer Institute, Minneapolis, 1990.

[16] F. Ilinca, D. Pelletier, and A. Garon, "An adaptive finite element method for a two-equation turbulence model in wall-bounded flows," *International Journal for Numerical Methods in Fluids*, vol. 24, pp. 101–120, 1997.

[17] L.P. Franca and S.L. Frey, "Stabilized finite element methods: II. The incompressible Navier-Stokes equations," *Comp. Methods Appl. Mech. Engng.*, vol. 99(2-3), pp. 209–233, 1992.

[18] Y. Saad, "Iterative Methods for Sparse Linear Systems," PWS Publishing Company, Boston, MA, 1996.

[19] H. Van der Vorst, "Bi-CGSTAB: A fast and smoothly converging variant of Bi-CG for the solution of nonsymmetric linear systems," *SIAM J. Sc. Stat. Comp.*, vol. 13, pp. 631–644, 1992.

[20] M.N. Linnick and H.F. Fasel, "A high-order immersed interface method for simulating unsteady incompressible flows on irregular domains," *Journal of Computational Physics*, vol. 204, pp. 157–192, 2005.

[21] Y. Cheny and O. Botella, "The LS-STAG method: A new immersed boundary/level-set method for the computation of incompressible viscous flows in complex moving geometries with good conservation properties," *Journal of Computational Physics*, vol. 229, pp. 1043–1076, 2010.

[22] A. Sohankar, C. Norberg and L. Davidson, "Low-Reynolds-Number Flow Around a Square Cylinder at Incidence: Study of Blockage, Onset of Vortex Shedding and Outlet Boundary Condition," *Int. J. Num. Methods Fluids*, Vol. 26, pp. 39–56, 1998.

[23] C. Liu, X. Zheng and C.H. Sung, "Preconditioned multigrid methods for unsteady incompressible flows," *Journal of Computational Physics*, vol. 139, pp. 35–57, 1998.

[24] A. Belov, L. Martinelli and A. Jameson, "A new implicit algortihm with multigrid for unsteady incompressible flow calculations," *AIAA 95-0049*, January 9-12, 1995.

[25] E.M. Saiki and S. Biringen, "Numerical Simulation of a Cylinder in Uniform Flow: Application of a Virtual Boundary Method," *J. Comp. Phys.*, vol. 123, pp. 450–465, 1996.

[26] O.M. Griffin and S.E. Ramberg, "Vortex shedding from a cylinder vibrating in line with an incident uniform flow," *J. Fluid Mech.*, Vol. 75, pp. 257–271, 1976.

[27] A. Ongoren and D. Rockwell, "Flow structure from an oscillating cylinder, Part 2. Mode competition in the near wake," *J. Fluid Mech.*, Vol. 191, pp. 225–245, 1988.

[28] C.-C. Liao, Y.-W. Chang, C.-A. Lin and J.M. McDonough, "Simulating flows with moving boundary using immersed-boundary method," *Computers & Fluids*, vol. 39, pp. 152–167, 2010.

[29] A. ten Cate, C.H. Nieuwstad, J.J. Derksen and H.E.A. Van den Akker, "Particle imaging velocimetry experiments and lattice-Boltzmann simulations on a single sphere settling under gravity," *Physics of Fluids*, Vol. 14, pp. 4012–4025, 2002.